2.1.3. The correlation dimension

The correlation dimension is derived from the correlation function, which describes the probability of finding a pair of points inside a hyper-cell of a dimension of r. For a set $\{x_i\}$ of n points, which are located at the distance of $s_{ij} = |x_i - x_j|$ the correlation function can be determined by the equation:

$$C(r) = \frac{1}{n(n-1)} \sum \left(\begin{array}{c} \text{number of pairs } (i, j) \\ \text{of a distance of } s_{ij} < r \end{array} \right) \tag{2.11}$$

The correlation function in the case of fractal object is scaled according to power law:

$$\lim_{\delta \to 0} C(r) = a \cdot r^D \tag{2.12}$$

Then the correlation dimension D_{CO} can be determined by the slope of the plot in log-log graph of the correlation function:

$$D_{CO} = \lim_{r \to 0} \frac{\log C(r)}{\log r} \tag{2.13}$$
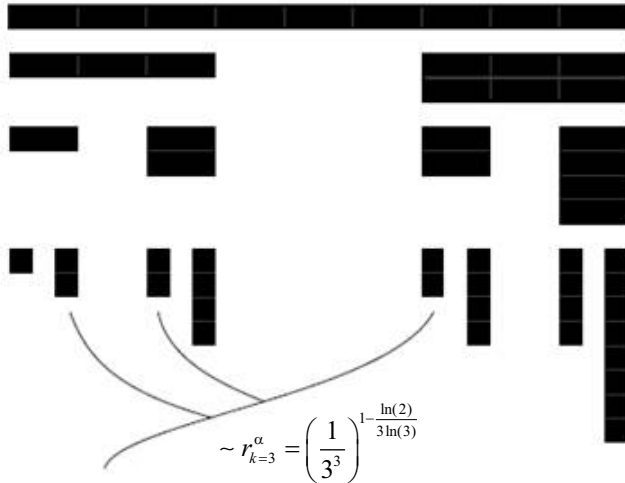
2.2. Basics of multifractal analysis

Classical fractals (monofractals), which were described in previous section, are mostly used for n-dimensional space, multifractals deal with measure. Measure, in this situation, is to be understood as a mathematical notion. In practice, data can be mathematical measures (for example a probability measure) or any value distribution that can be transformed into a measure (for example, a weighted set, fractal landscape, time series) [23]. At the root of the idea of multifractality is the desire to study the complexity and reveal the scaling properties of a mathematical object as well as self-similarity. Measure (for example, a set or time series) can be a multifractal despite its support being a monofractal. To explain multifractal analysis, there is a need for a subset $D \subset \mathbb{R}^n$, on which a "fractal" measurement method M and a finite measure μ are defined.

M – can be any method which can be used to calculate a monofractal dimension (examples of these methods are presented in Section 2.1). A multifractal measure μ on subsection D is a distribution such that around any $x \in D$, for the measure in the shape of a ball of radius r around point x, is scaled with r, which means it is proportional to r^α for some α, provided that r is small enough. In this way, sets of points, created by all points, which are located around which the scaling exponent is the same, are monofractals for M. The fractal dimension of the set which corresponds to a local exponent α is usually denoted as $f(\alpha)$.

Most fractal methods of measure M are based on defining self-similar local measurement M_r, (such as the number of boxes which are required to cover the set for box-counting dimension). The multifractality μ, in that case, is characterized by a distribution such as the two following fundamental scaling relations which hold for small enough r:

- $\mu_r(x) \sim r^{\alpha_x}$ for α_x around any $x \in D$, where $\mu_r(x)$ is a measure in a ball of radius r around r;
- $M_r(\alpha) \sim r^{-f(\alpha)}$ for $f(\alpha)$, where $M_r(\alpha)$ is the M_r – measurement of the set $\{x, \alpha_x = \alpha\}$.

The multifractal spectrum is a dependence graph of $f(\alpha)$ against α. It contains information about sets where the measure scales locally with the same scaling exponent α. Multifractal analysis should be understood as a method which is used in order to characterise and for comparison of measures defined on set D, when the measures have enough scaling properties to alleviate the internal complexity of (D, μ).

$$\sim r_{k=3}^{\alpha} = \left(\frac{1}{3^3}\right)^{1-\frac{\ln(2)}{3\ln(3)}}$$

Fig. 2.2. Weighted multifractal middle third Cantor set, first three iterations [23]

An example of multifractal analysis is presented in Figures 2.2 and 2.3. The weighted multifractal middle third Cantor set is made by dividing the set into three segments of the same length, and the middle segment is removed. Additionally, the right segment is weighted twice as much as the left one in each step. First, three iterations of this process are presented in the Figure 2.2. The size of the new sub-segment at iteration k is described by the r_k symbol, and it is assumed that for $r_0 = 1$. By doing it in that way, 3^k of sub-segments are obtained. For example, for the iteration $k = 3$, as in this example presented in the Figure 2.2, 27 segments of different heights are obtained, each of size $r_3 = (1/3)^3$ and carrying a weight of r_3^{α} for some α. At the macroscopic state, a broad method M can be defined such that $M_{rk}(\alpha)$ denotes the number of sub-segments which are scaled with r_k for an exponent α. This number can be expressed as $r_k^{-f(\alpha)}$. For α chosen in the Figure 2.2 ($\alpha = 1 - (\log 2)/(3 \cdot \log 3)$), there are $3 = (1/3^3)^{-1/3}$ sub-sections carrying the same measure. For this reason, the fractal dimension of such a subset is: $f(\alpha) = 1/3$. After repeating the calculations above for each of four different weights carried by the sub-sections at iteration $k = 3$, the spectrum is obtained (bottom line in the Figure 2.3).

For such a low iteration, M does not have much sense, but when $k \to \infty$ the spectrum obtained converges to the spectrum that would be obtained for the Hausdorff measure for the weighted middle third Cantor set.

Two variants of spectra are distinguished by Falconer [22]: the singularity spectrum and the coarse spectrum. The singularity spectrum is the most canonical definition and includes

the universality which is often sought in mathematics. The coarse spectrum, on the other hand, approximates the singularity spectrum and is often used in practice.
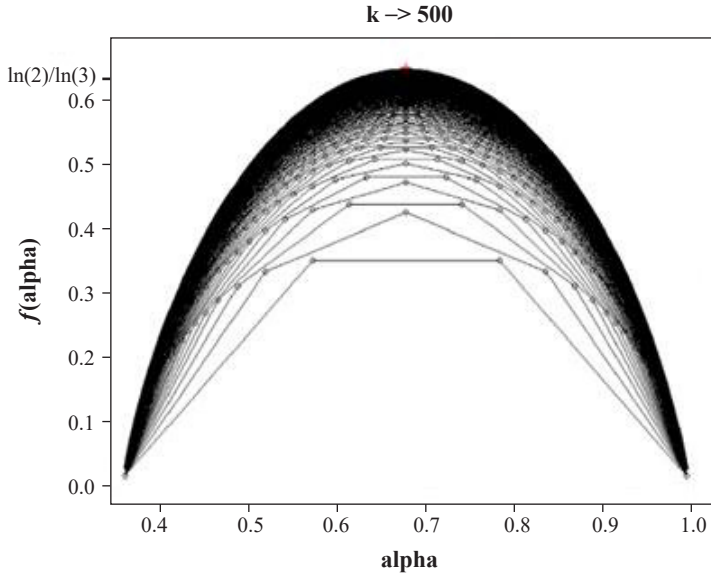
Fig. 2.3. Multifractal spectrum for the 500 iterations of weighted multifractal middle third Cantor set [23]

The singularity spectrum is defined in a following way. The topological space D and a finite measure μ is found on the topological space D. The local scaling exponent α_x of the measure μ for $x \in D$ is given by the Hölder dimension $\dim_{loc}$, which is defined by Dependence (2.14):

$$\dim_{loc} \mu(x) := \lim_{r \to 0} \frac{\log \mu(B(x,r))}{\log r} \tag{2.14}$$

where $B(x, r)$ is a ball of a centre in x and radius of r for the topology of D. Thus, the singularity spectrum f_H is defined by following equation:

$$f_H(\infty) := \dim_H \{x \in D, \ \dim_{loc} \mu(x) = \infty\} \tag{2.15}$$

where $\dim_H$ is the Hausdorff dimension.

If a grid of a size r, which covers the space D, is taken into consideration and the number of cells for which μ is r^α, then the function of number of cells equals:

$$N_r(\infty) := \#\{i : \mu(C_i) \geq r^\infty\} \tag{2.16}$$

where:

$\#$ – number of the cells,

C_i – a cube made from grid of cell size r.

The probability of the collision of particles of a solid phase, which have a density almost identical to the fluid, depends on the velocity of the Brownian motion, and this depends on the temperature and the viscosity of the fluid, and also the intensity at which the suspension moves. The intensity of the movement of suspension can be manipulated by the type of flow through the system of transportation of the suspension or the type of mixing. Aggregation, which is caused by Brownian motion, is named perikinetic aggregation and was described by Smoluchowski. He estimated the decrease of the number N_1 of single, small monodisperse particles at the beginning of aggregate formation during collisions per time unit; this can be described by the equation:

$$\frac{dN_1}{dt} = -4\pi R D_{11} N_1^2 \tag{3.2}$$

where:

R — the radius of influence of the particle,
D_{11} — the diffusion coefficient of two identical particles between them.

Integrating this equation gives the number of particles which are not yet aggregated after time t:

$$N_1 = \frac{N_0}{1 + 4\pi R D_{11} N_0 t} = \frac{N_0}{1 + 8\pi R D_0 N_0 t} \tag{3.3}$$

where:

N_0 — the number of particles at the beginning of the aggregation process ($t = 0$) in one unit of volume of suspension,
D_0 — the diffusion coefficient.

The diffusion coefficient can be calculated from following equation:

$$D_0 = \frac{R_G T}{3\pi\mu d N_A} \tag{3.4}$$

where:

R_G — gas constant,
T — absolute temperature,
μ — the dynamic viscosity coefficient,
d — the diameter of particle,
N_A — Avogadro constant.

After the transformation of equation 3–3, one can obtain dependence for the time of coagulation of $N_0 - N_1$ particles which will aggregate:

$$t = \frac{1}{8\pi R D_0}\left(\frac{1}{N_1} - \frac{1}{N_0}\right) \tag{3.5}$$

The experimental validation of the dependence was made by Smoczyński [49] among others.

The creation and disintegration of aggregates is connected not only with physicochemical dependences between particles, but also with the movement of the suspension. The movement of suspension can be induced by its flow or mixing. The process of suspension stirring greatly increases the aggregation rate, which is caused by the existing in such case fluid velocity gradient. This kind of aggregation is called orthokinetic aggregation (presented in the Figure 3.4). By ignoring the influence of the repulsive forces, the formula describing this type of aggregation takes the following form:

$$\frac{\mathrm{d}N_1}{\mathrm{d}t} = -\frac{16}{3}\gamma_t R^3 N_1^2$$

(3.6)

where:

γ_t – the fluid velocity gradient, shear rate ($\gamma_t = \mathrm{d}U/\mathrm{d}z$),
R – the radius of influence of the particle.
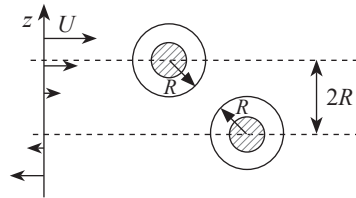
Fig. 3.4. Chart of orthokinetic collision of particles in the shape of balls (hatched area) in laminar shear flow (R – radius of influence of the particle)

In the case when there are mixed particles with two different radii of influence in the suspension (this is the so-called bi-disperse system), Equation (3.6) will take following form:

$$\frac{\mathrm{d}N_1}{\mathrm{d}t} = -\frac{4}{3}\gamma_t N_1 N_2 (R_1 + R_2)^3$$

(3.7)

where:

R_1, R_2 – the radius of influence of a given particle,
N_1, N_2 – the number of particles with the radius of influence R_1, R_2, which are not aggregated in one unit of suspension.

Because not all collisions during mixing lead to an aggregation of particles, a reduction factor is often introduced. In the case of a bi-dispersion system, the recommended value of the velocity gradient can be estimated from the following equation:

$$\gamma_t = \sqrt{\frac{\varepsilon^*}{\mu_m}}$$

(3.8)

where:

ε^* – the energy dissipation speed,
μ_m – the dynamic viscosity of the suspension.

The Reynolds number, which describes the ration of inertia forces to viscosity, can be represented by the Relation (4.4):

$$Re = \frac{v_s d}{v} = \frac{v_s d \rho_f}{\mu_f}$$

(4.4)

where:

v_s — the terminal velocity of the particle,
v — the coefficient of kinetic viscosity,
μ — the coefficient of dynamic viscosity.

The general equation of motion of a viscous fluid is as follows:

$$\rho_f \frac{\partial u_f}{\partial t} + \rho_f \cdot u_f (\nabla u_f) = -\mathrm{grad}\, p_f + \mu \nabla^2 u_f + \rho_f g$$

(4.5)

where:

u_f — the flow velocity,
p_f — the pressure of the fluid,
∇ — Nabla operator,
∇^2 — Laplace operator.

In Equation (4.5), the influence of the inertia forces is described by the expression $\rho_f \cdot u_f(\nabla u_f)$. Assuming that the flow velocity is constant, i.e., $\partial u_f / \partial t = 0$ and neglecting the effects of inertia forces (the expression $\rho_f \cdot u_f(\nabla u_f)$), the equation is simplified to the form:

$$\mathrm{grad}\, p_f = \mu \nabla^2 u_f + \rho_f g$$

(4.6)

This form of the equation of fluid flowing around a sphere with flow velocity of u_f was considered by Stokes. The velocity of the fluid flowing around the spherical particle u_f can be interpreted as equal to the velocity of the spherical particle in the stationary fluid (or the terminal velocity of the free-falling spherical particle v_s)

The equation for calculating the drag force F_D was one of the results of Stokes considerations. The drag force can be obtained from following equation:

$$F_D = 3\pi\mu d v_s$$

(4.7)

This relationship is called the Stokes law: In a steady flow, the resistance force of a stationary fluid to a falling particle is proportional to the terminal velocity of particle v_s and to its size d.

On the other hand, the drag force of a viscous medium, i.e., the force opposing the flow of a particle, according to the Newton equation is given by the formula:

$$F_D = \Psi \cdot F_{CZ} \frac{v_s^2}{2} \rho_f$$

(4.8)

where F_{CZ} is the projected area of the perpendicular surface of the particle to the movement of the particle.

Comparing the drag force for a spherical particle from Equations (4.7) and (4.8) one can get:

$$3\pi\mu d v_s = \Psi \cdot \frac{\pi d^2}{4} \frac{v_s^2}{2} \rho_f \qquad (4.9)$$

From this comparison it is possible to calculate the drag coefficient ψ, correct for the so-called "small" Reynolds numbers $10^{-4} < Re < 0.25$:

$$\Psi = \frac{24}{Re} \qquad (4.10)$$

In matters related to the design of environmental protection devices and processed, the right boundary of the Formula (4.10) is extended to Reynolds number $Re = 2$, if in practical matters the flow around the particle will slightly differ from the laminar flow, and the resulting errors are not great.

The dependence of the drag coefficient ψ on the Reynolds number (Re) is given in Figure 4.3 There are three zones (I, II and III). Each of the zones corresponds to the effects of different type of flow: I – laminar flow, II – transitional flow, III – turbulent flow.
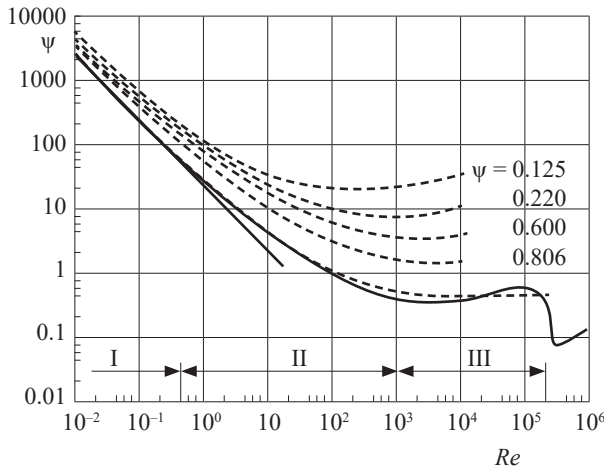
Fig. 4.3. Dependence of drag coefficient from Reynolds number during particle sedimentation: I – laminar flow, II – transitional flow, III – turbulent flow [75]

The terminal velocity for these three zones can be calculated by inserting a drag coefficient into Equation (4.3).

Thus, for the free-falling particle within laminar flow, it is possible to use the widely used Stokes formula:

$$v_s = \frac{1}{18} \frac{\rho_s - \rho_f}{\mu} g d^2 \qquad (4.11)$$

4.4. Sedimentation process of non-grainy particles – classical approach

The process of sedimentation of a grainy suspension is different from the process for non--grainy suspensions. This is due to the huge difference in the structure of the particle under consideration. The terminal velocity for grainy particles is unchanged and remains constant, while for non-grainy particles, the terminal velocity initially increases as a result of agglomeration of the particles; however, it is not necessarily constant. This kind of situation is presented in the Figure 4.4.
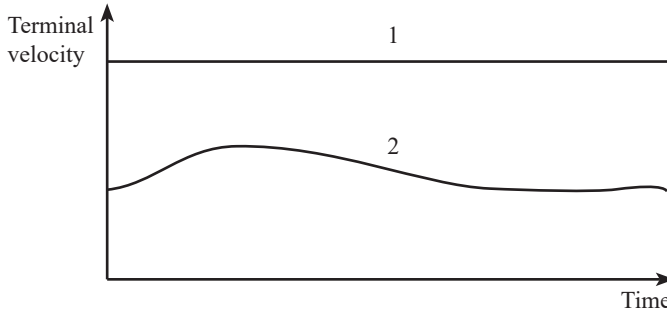
Fig. 4.4. Terminal velocity of particles as a dependence of time:
1 – monodispersed grainy suspension, 2 – non-grainy suspension [48]

Removal efficiency of suspension is most often determined in specialized laboratories based on various tests (sedimentation tests, tests of active substances applied to a given suspension or tests of multi-flux lamella packets) depending on the needs (for example, whether additional installation of multi-flux lamella packets or use of chemical additives is justified, and also if it is possible to apply such solutions or what benefits or drawbacks solutions may bring).

Particles of clay minerals with diameters of $0.1 < d < 30$ μm and with concentration of 10 kg/m^3 in seawater with a salt concentration of 30‰ according to [77] form flocs with an average settling velocity greater than the settling velocity of a single particle, the smaller is the average diameter d_{50} of these particles, for example:

$$\frac{v_{kn50\%}}{v_{1n50\%}} \approx \frac{250}{d_{50}^{1.8}} \approx \left(\frac{20}{d_{50}}\right)^2 \tag{4.15}$$

where:

$\quad v_{kn50\%}$ — the average free-falling velocity of flocs composed of individual, fine particles,

$\quad v_{1n50\%}$ — the average free-falling speed of the individual particles from which the floc is made,

$\quad d_{50}$ — the average diameter of the individual particles in the suspension.

The length of the clay particles may vary. The largest one can be up to several centimetres. The effective density of such structures, due to the high porosity, tends to the density of the dispersing phase. As a result, the average free-falling velocity of such particles is low and that is why suspensions of clay minerals and other non-grainy suspensions are usually hard to settle – the particles show resistance to the process of sedimentation.
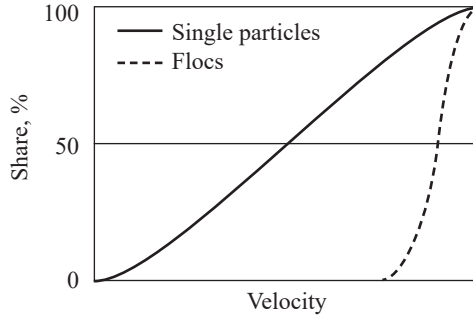

Fig. 4.5. Graph of the velocity of single particles and flocs [48]

Generally speaking, independent, individual flocs will fall faster than the single, fine particles which form the flocs; this situation is presented in the Figure 4.5. However, it should be borne in mind that a large number of flocs in a limited volume will limit their falling speed. The changes of concentration of dry matter during that process are presented in Figure 4.6.
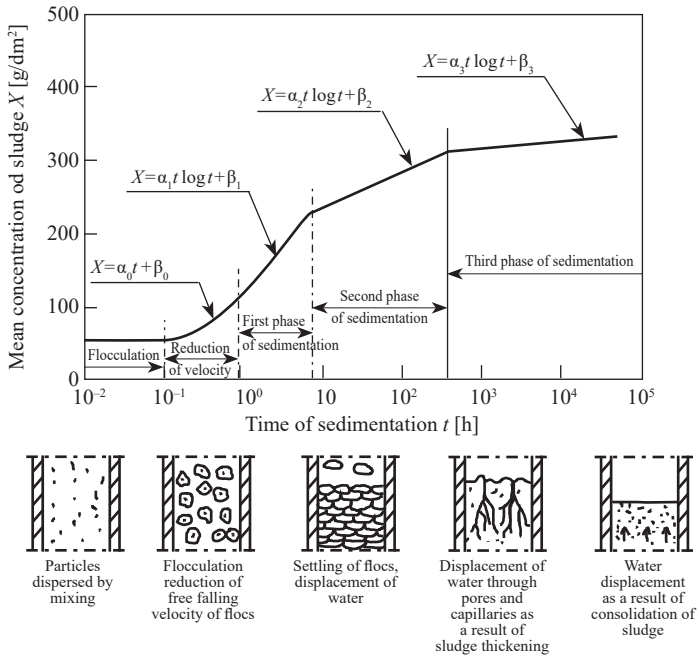

Fig. 4.6. Changes in the concentration of dry matter of sludge [48]

One of the sedimentation models of non-grainy suspension is the activated sludge floc sedimentation model developed by Cho [78]. It is represented by the following equation:

$$\frac{\Delta p}{L} = \phi(\rho_s - \rho_m)g = \phi(1-\phi)(\rho_s - \rho_f)g \qquad (4.16)$$

where:

ρ_s – the density of the particle,
ρ_m – the density of the suspension,
ρ_f – the density of dispersing phase,
ϕ – the volume concentration of solid particles,
L – thickness.

In this model, it was assumed that the movement of the layer of thickness L is equivalent to the filtration through the same layer with a pressure gradient $\Delta p/l$, which results from the weight of the flocs subtracting their buoyancy. You can compare this pressure gradient to a gradient calculated from the Kozeny–Carman formula:

$$\frac{\Delta p}{L} = \frac{\phi^2}{(1-\phi)^3} v_z K \mu_m a_{wk}^2 \qquad (4.17)$$

where:

v_z – the velocity of the free falling of sediment layer in the case of constrained sedimentation,
K – constant which equals 4.167,
μ_m – the dynamic viscosity of the suspension,
a_{wk} – the specific surface area of the flocs in squar meters per cubic meters, it may have different values.

Using these two Equations (4.16) and (4.17), the following equation can be obtained after transformation:

$$v_z = \frac{(\rho_s - \rho_f)g}{K\eta_m a_{wk}^2} \frac{(1-\phi)^4}{\phi} \qquad (4.18)$$

By changing the volume concentration of hydrated floc to bulk concentration, by substituting:

$$\phi = nX \qquad (4.19)$$

is obtained:

$$v_z = k \frac{(1-nX)^4}{nX} \qquad (4.20)$$

where:

k – the empirical coefficient which equals 20–32 kg/(m$^2 \cdot$h),
X – the concentration of activated sludge,
n – the empirical coefficient (range 0.044–0.059 m^3/kg).

The first practical attempts to measure turbidity date back to 1900, when Whipple and Jackson developed a standard suspension which consisted of diatomaceous earth at a concentration of one thousand parts per million (ppm) in distilled water. Then various dilutions of this suspension produced a series of standard suspensions, which were then used to determine the scale of silica concentration (in parts per million) and thus the first turbidity curve (the dependence between turbidity and concentration of a suspension).

The first basic method for determining turbidity was the method based on the Jackson turbidimetric candle using the ppm scale of Whipple and Jackson silica. Turbidity measured by this method is expressed in the Jackson Turbidity Unit (JTU). The standards were prepared from naturally occurring materials such as Fuller's earth, porcelain clay, deposits of sediments; therefore, the consistency and coherence of this preparation was difficult to achieve each time.

In 1926, formazine was discovered by Kingsbury and Clark; they used it to prepare calibration standards which significantly improved the consistency and the repeatability of the turbidity tests. Formazine was prepared from carefully measured 5 grams of hydrazine sulphate and 50 grams of hexamethylenetetramine, which were then diluted in one litre of distilled water. This suspension is commonly used in turbidity standards. The formazine turns white after standing at 25ºC for 48 hours. The name of the turbidity unit of measure that uses formazine as a standard to determine the turbidity level is FTU (Formazin Turbidity Unit).

Although the invention of formazine significantly improved the accuracy of the Jackson turbidimeter, the measurement of high and low turbidity values was still impossible due to the lack of adequate precision. For Jackson's turbidimeter, the lowest measurable turbidity value is 25 JTU.
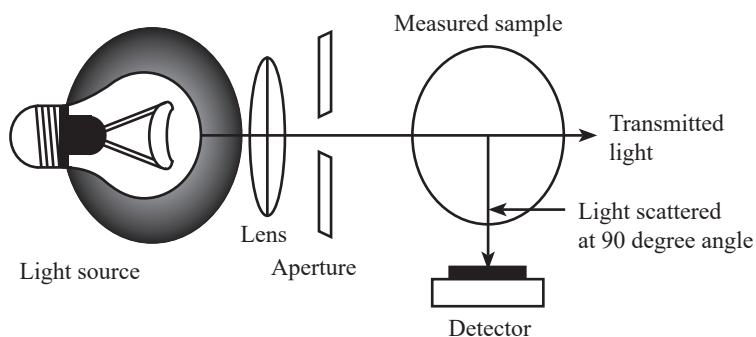
Fig. 5.2. The principle behind the nephelometric measurements [89]

Indirect methods have been developed to improve the determination of low turbidity. Several new turbidimeters, equipped with better light sources and measurement and comparison techniques, were developed, but still these devices were too dependent on the human eye and perception. In the late 1970s, a more accurate nephelometric turbidimeter was developed. The principle behind the nephelometric measurements is presented in the Figure 5.2. The nephelometric turbidimeter determines the turbidity from the light reflected at a 90º angle from the incident beam. The detection angle of 90º is the least sensitive to changes that

may be caused by particle size. Nephelometry has been adopted as the preferred method of measuring turbidity due to the sensitivity and accuracy of the method and the wide range of concentration and particle sizes in the tested suspensions. Current calibration standards are also made from formazine polymer.

Light scattering on fine particles

The interactions between light radiation and suspended solid particles are presented in Figure 5.3 and can be divided into four types:
1) diffraction on particles' outlines,
2) reflection on the particles' surfaces (both internal and outer surfaces),
3) scattering on the particle-liquid interface,
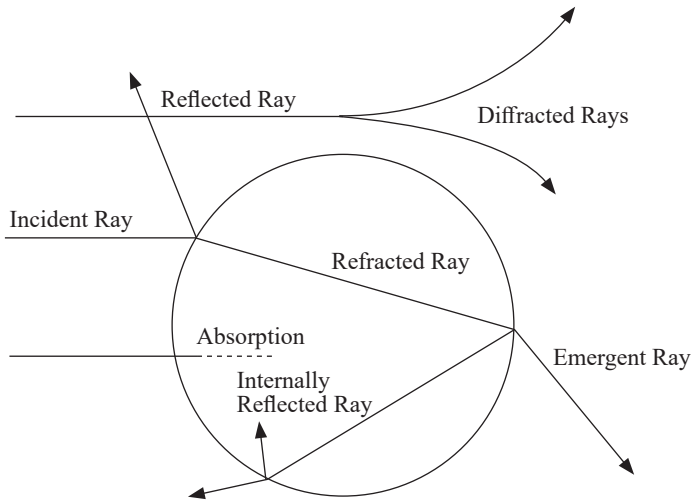4) radiation absorption inside the particle.

Fig. 5.3. Types of interactions between light radiation and particles [4]

The intensity of the focused beam passing through the suspension is reduced depending on the type of the interaction between radiation and particles (some of them will have a greater or lesser impact – for example, the diffraction of light beam on particles' outline which depends on the type of particle and the physical properties of the substance of the particle). In general these, phenomena are known as light scattering.

Diffraction of radiation is the most important phenomenon causing the scattering of the light beam. The particle size has a significant influence on the angle and the intensity of the diffraction. Larger particles scatter radiation at small angles, and quite often absorption of radiation occurs in such particles, for smaller particles the light beam is deflected at larger angles. Due to the difference in light intensity caused by scattering an image of so-called diffraction patterns on particles, which is formed at a certain distance from the particle. The appearance of such patterns will depend on the size, shape and optical properties of the particles on which the light beam has refracted. Examples of diffraction patterns are shown in the Figure 5.4.

# 6.1. Characteristics of tested material

Bentonite is a clay mineral with unique properties [107, 108]. Bentonites are formed from the transformation of enamel found in ash and volcanic tuffs. They are composed mainly of minerals from the smectitce group (mainly montmorillonite), accompanied by other minerals (such as sanidin, biotite, quartz, heavy minerals, volcanic glaze, zeolites). It can be white, grey, yellow or brown, the most common varieties are grey.

From the point of mineral composition, montmorillonite and smectite minerals have the greatest impact on the properties of bentonites, which determine the most important properties of bentonite, such as plasticity, swelling ability, sorption capacity and strong absorption properties. When bentonite has access to moisture, it swells by accumulating water particles in the inter-layer space, increasing their volume several times. Sodium bentonite (Na-montmorillonite) has the highest water adsorption capacity.

Bentonites come in many varieties; due to their structure they are also susceptible to various modifications, such as: alkaline, acidic, thermal, or organic activations. Due to its properties, bentonite is used in many industries; therefore, it is possible that solid bentonite particles can be found in water, which is further used, for example, in water treatment plants.

This mineral is characterized by a 2:1 layered structure. This structure consists of two tetrahedral sheets and one octahedral sheet. In the dry state, bentonite has a certain mechanical strength; however, while in contact with water, the structure breaks down due to the absorption of water and ions dissolved in water in the spaces between the layers.

Due to the presence of negative and positive unsaturated charges on individual layers, bentonites in suspension tend to form a structure like a house of cards. The presence of uncompensated charges on surface of the layers of clay materials; they are also characterized by the possibility of easily adopting liquids (for example water) into their structure, and they can also substitute cations such as sodium and limestone. During the sedimentation process, they can combine with each other to form particles of complex, flocculent structures, which can be difficult to remove from liquid. Examples of structures that can be formed by this type of particles are shown in Figure 6.1.
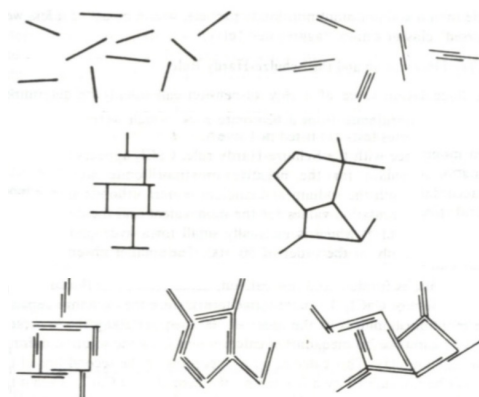
Fig. 6.1. Examples of different structures that can be formed from clay mineral layers, by joining with flat surfaces, edges, and corners

6.1.1. Mineralogical identification of bentonite samples

As part of this study, chemical and mineralogical identification of solid phase samples, for which further tests were carried out, was performed. Three samples of Slovak bentonites from Certech company were named S1 – S3, depending on the amount of montmorillonite. The samples were ground and dried in dry-air conditions then preliminary analyses were performed on them:
- chemical composition analysis by the method of atomic emission spectroscopy with plasma excitation (ICP-AES ELAM 6100);
- phase composition analysis by X-ray method (PHILIPS APD X-Pert PW3020);
- scanning microscope analysis (HITACHI SU-70 and JEOL 5500 LV with EDS system of company IXRF).

6.1.2. SEM imaging of bentonite samples

Information on the particle shape of solid phase bentonites S1 – S3 was obtained from a scanning microscope. The Figures 6.2–6.4 show, that the particles that make up these samples are grains with significantly different shapes from the spherical shape. Additionally, their sizes are in a wide range, from several to several dozen micrometers.
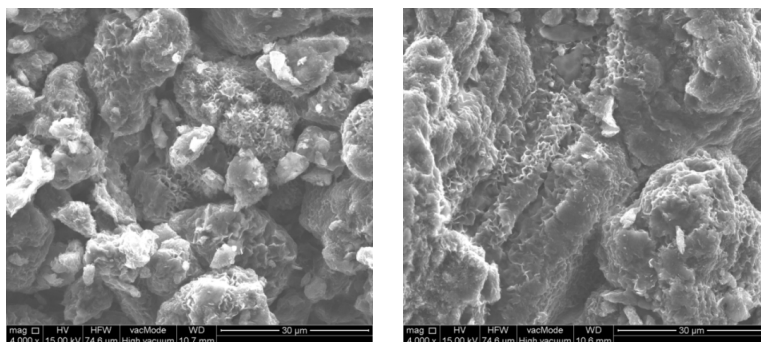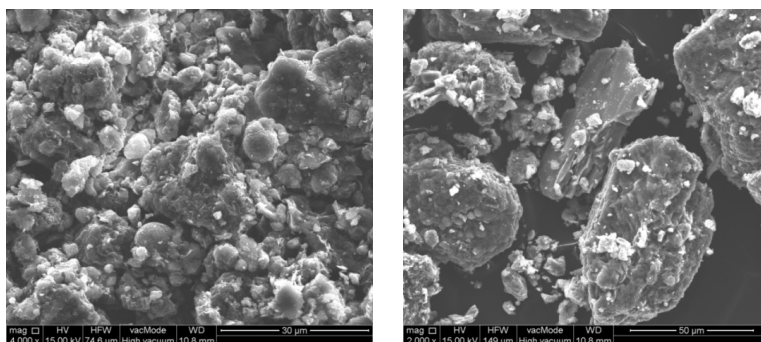

Fig. 6.2. SEM images for sample S1

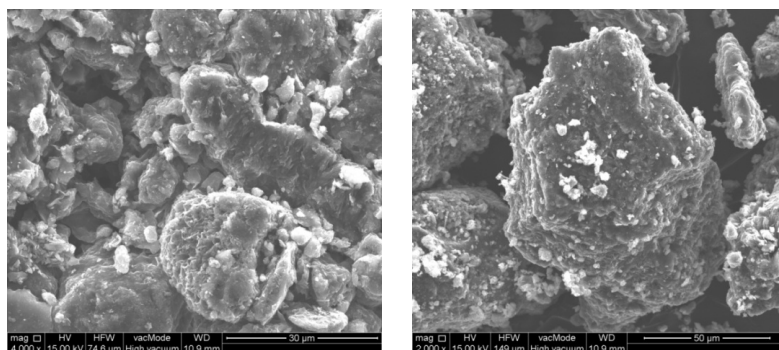
Fig. 6.3. SEM images for sample S2

Fig. 6.4. SEM images for sample S3

6.1.3. Chemical composition

The chemical composition of bentonites under investigation is presented in Table 6.1.

Table 6.1

Chemical composition of bentonites under investigation

Component [%]	S1	S2	S3
MgO	2.825	1.630	1.543
Al_2O_3	31.675	20.400	21.103
SiO_2	59.245	70.856	71.960
K_2O	0.600	1.076	1.113
CaO	2.360	1.960	1.423
Fe_2O_3	3.295	4.076	2.860

Presented results show that in the tested bentonites, sillica (SiO_2) is the dominant material in terms of chemical composition (the highest content of sillica is in the sample S3). Moreover, aluminium (aluminium oxide Al_2O_3) is present in the analysed samples with the highest content present in sample S1. In addition, calcium, iron, potassium, and magnesium were also found in small amounts (about 2–4%). The content of other elements is less than 1%. These results were supported by the results from the phase analysis.

6.1.4. Phase composition

The phase composition of bentonites is presented in the form of graphs (in Figures 6.5–6.7) and in a Table 6.2.

Montmorillonite $(Na,Ca)_{0.3}(Al,Mg)_2Si_4O_{10}(OH)_2 \cdot n(H_2O)$ with the highest content in the S1 sample (90–98%) is the dominant mineral in all bentonites. In samples S2 and S3, montmorillonite was identified in smaller amounts. In all samples, other clay minerals (illite and muscovite) were additionally identified.

6.2.2. Particle size distribution –
   ### measurement by laser diffraction

The particle size distribution of the bentonite suspension samples was also tested on Master-Sizer 2000E laser diffractometer equipped with a Hydro Mu wet sample dispersion unit. The analyser allowed us to determine particle size distribution in dispersion systems in the range from 0.1 to 1000 µm.

The multiangle laser light scattering technique (MALLS) is the principle behind the MasterSizer 2000E analyser. The source of laser radiation is a helium-neon laser with a wavelength of $\lambda = 633$ nm. The analyser is equipped with 44 light radiator sensors set at angles from 0.01° to 40.61°, of which the first 33 sensors are low-angle sensors (positioned on a plate behind the measuring cell), while the remaining sensors are high-angle sensors. The diagram of the analyser is shown in Figure 6.11.
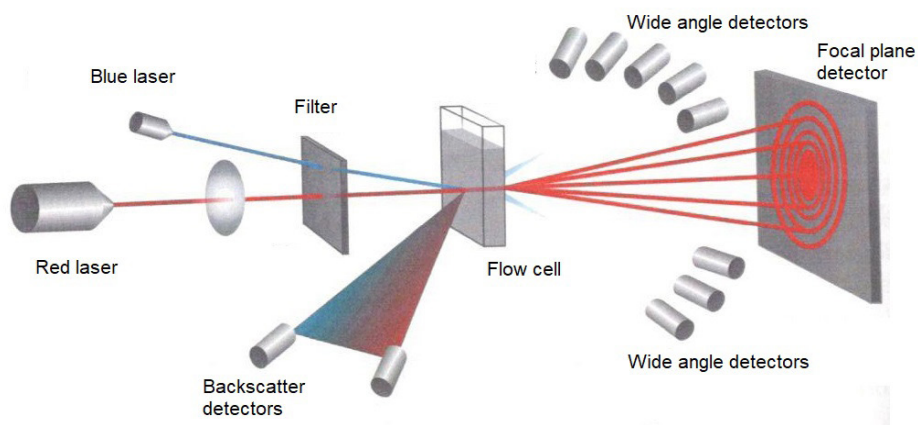

**Fig. 6.11.** MasterSizer 2000E diffractometer

Measurement in the MasterSizer2000E diffractometer consists of directing the emitted laser light beam focused by the Fourier lens at the measuring cell, through which the suspension, subjected to granulometric analysis, is constantly transported (from the bottom to the top of the measuring cell). The particles of the suspension scatter the laser light at certain different angles, which are then picked by the sensors, which measure the intensity of the laser light. The set of indications from all (44) sensors, called "flash", is registered with a frequency up to 10,000 per second and uploaded to the controlling computer. On the computer specialized software that controls the operation of the analyser and processes the indications of the sensors is installed. The software can process the indications of the sensors to determine the size of the particles in the suspension, using selected scattering model (extended Mie theory or the simplified Fraunhoffer model). The type of the dispersion unit influences whether the measurements can be taken in liquids and in a gaseous phase.

In the tests, the HydroMU unit was used. It is designed for measurement in liquids of large volumes (up to 1 dm³), and it is equipped with a rotor pump operating at 800–4000 rpm. The ultrasonic disintegrator is also an integral part of the HydroMu dispenser.

6.2.3. Results of measurements of particle size distribution of bentonite suspensions

The measurement of particle size distribution on the diffractometer was performed for each sample as follows. 500 cm^3 of demineralised and degassed water was poured into the beaker of the wet dispersion unit, then the sample, in a loose form, was added to the beaker is such quantity as not to exceed the required threshold of obscuration (between 10% and 20%). The bentonite suspension, prepared in this way, was also homogenized in the beaker by mixing it at a speed of 2000 rpm. The measurement was repeated 5 times to minimize errors. The particle refractive index was set at 1.61, and the absorption index was set at 0.1, according to the instructions supplied with the device. The results of the particle size distribution are presented in Figures 6.12–6.14.
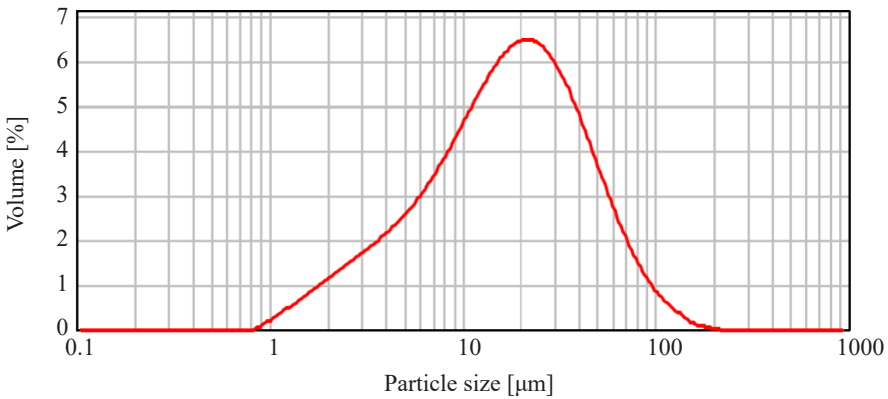
Fig. 6.12. Particle size distribution of suspension S1.
Characteristic particle sizes for sample S1 are as follows:
$d_{50} = 17.5$ μm (median), $d_{10} = 3.9$ μm, $d_{90} = 52.3$ μm
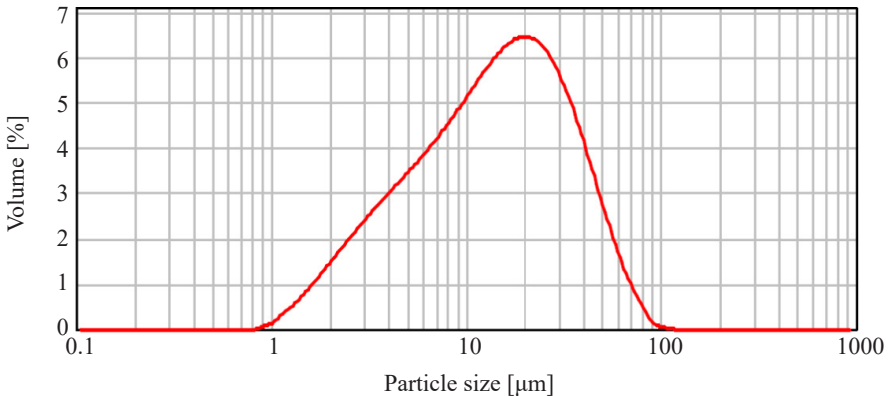
Fig. 6.13. Particle size distribution of suspension S2.
Characteristic particle sizes for sample S2 are as follows:
$d_{50} = 14.2$ μm (median), $d_{10} = 3.3$ μm, $d_{90} = 40.1$ μm

6.5.1. Laboratory stand – model of sedimentation tank equipped with multiflux lamella packet

The sedimentation efficiency is a parameter that determines the degree to which solid particles are removed from suspension. Usually, this parameter is determined experimentally in model sedimentation tanks, which can be made in various sedimentation variants. This chapter presents measurements of sedimentation efficiency in a settling tank with packets in the counter-current sedimentation variant.

The settling tank with a multi-flux lamella packet is divided into three chambers: a priming chamber, a sedimentation chamber (where the multi-flux lamella packet can be inserted at an angle of $60°$) and an overflow chamber. Total sedimentation area of the settling tank is 210 cm². The test stand for the settling tank is shown in Figure 6.22.
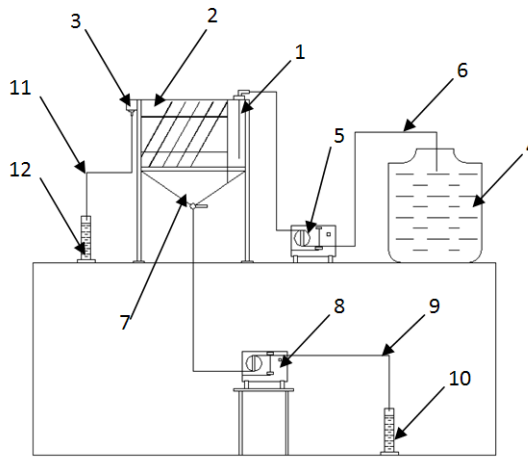

Fig. 6.22. Test stand for sedimentation process under flow condition:
1 – priming chamber; 2 – sedimentation chamber with multi-flux lamella packet; 3 – overflow chamber; 4 – supply tank with an agitator; 5, 8 – peristaltic pumps; 7 – collector chamber; 6, 9, 11 – peristaltic hoses; 10 – underflow collection (precipitate collection); 12 – overflow collection

The test was carried out in such a way that in the supply tank (4), the prepared suspension was constantly mixed in order to uniform suspension under investigation. From the supply tank, the suspension was pumped by a peristaltic pump to the priming chamber of the settling tank (1). After the process of sedimentation, the clarified suspension was collected in the overflow (3), while the sediment was collected in the collector chamber (7) and then removed from the settling tank by peristaltic pump (8).

The real surface load was determined by measuring the filling time of a measuring cylinder at underflow collection (10) and overflow collection (12). The efficiency of sedimentation of the settling tank was determined by comparing the turbidity of the raw suspension taken from the tank (4) and the turbidity of suspension after the process of sedimentation in the overflow (12). The turbidity measurements were conducted after the flow had stabilized (by waiting for a change of the suspension in the settling tank twice). The turbidity of the raw

suspension and the overflow was determined using Turb 555IR and Turbidirect turbidimeters (for each point, a measurement was taken 5 times and the results were averaged). The results are shown in Figures 6.23–6.25.
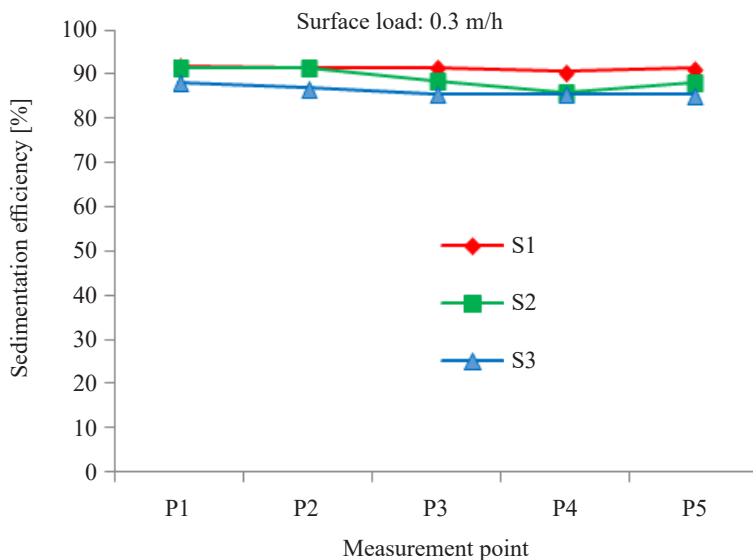
Fig. 6.23. Sedimentation efficiency for surface load of 0.3 m/h
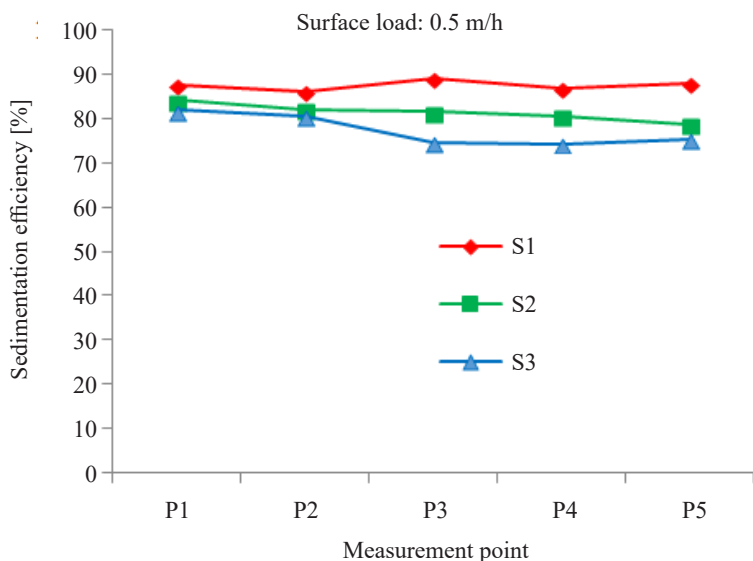
Fig. 6.24. Sedimentation efficiency for surface load of 0.5 m/h